Characterization of lithium phosphorus oxide thin film libraries by Laser-Induced Breakdown Spectroscopy imaging: A step towards high-throughput quantitative analyses

William Berthou, Maxime Legallais, Bruno Bousquet, V. Motto-Ros, Frédéric Le Cras

To cite this version:

William Berthou, Maxime Legallais, Bruno Bousquet, V. Motto-Ros, Frédéric Le Cras. Characterization of lithium phosphorus oxide thin film libraries by Laser-Induced Breakdown Spectroscopy imaging: A step towards high-throughput quantitative analyses. Spectrochimica Acta Part B: Atomic Spectroscopy, 2024, 215, pp.106906. 10.1016/j.sab.2024.106906 . cea-04529021

HAL Id: cea-04529021

https://cea.hal.science/cea-04529021v1

Submitted on 2 Apr 2024

Spectrochimica Acta Part B: Atomic Spectroscopy 215 (2024) 106906

Contents lists available at ScienceDirect

Spectrochimica Acta Part B: Atomic Spectroscopy

journal homepage: www.elsevier.com/locate/sab

Characterization of lithium phosphorus oxide thin film libraries by laser-induced breakdown spectroscopy imaging: A step towards high-throughput quantitative analyses

William Berthou[a,b], Maxime Legallais[a], Bruno Bousquet[b,**], Vincent Motto-Ros[c], Frédéric Le Cras[b,d,*]

[a] *CEA, CEA Tech Nouvelle Aquitaine, F-33600 Pessac, France*
[b] *Univ. Bordeaux, CNRS, Bordeaux INP, ICMCB, UMR 5026, F-33600 Pessac, France*
[c] *Univ. Lyon, Université Claude Bernard Lyon 1, CNRS, UMR5306, Institut Lumière Matière, Villeurbanne F-69100, France*
[d] *Univ. Grenoble Alpes, CEA, LITEN, DEHT, 38000 Grenoble, France*

ARTICLE INFO

Keywords:
LIBS
Chemical imaging
Thin films
High throughput experiment
Quantitative analysis
Lithium phosphate
Lithium batteries

ABSTRACT

Elemental analysis is a challenge for the development of High Throughput Experimentation (HTE) on thin film materials, and an even greater one when it comes to screening lithium-containing battery materials. In this regard, Laser-Induced Breakdown Spectroscopy has been evaluated here for the quantitative analysis of lithium in libraries of $Li_{2.3}PO_{3.65}$ amorphous solid electrolyte films. The LIBS analysis of multiple samples with the same composition, but with thicknesses ranging from 50 to 700 nm, has revealed a linear trend in the intensity ratio of the Li I 610.35 nm and P I 214.91 nm emission lines, opening the way to rapid quantitative analysis of material libraries. The sensitivity of the technique finally allowed the detection of the Li I 670.79 nm emission line for film thicknesses down to 4 nm, corresponding to 0.2% of the ablated volume, or about 0.15 pg of Li.

1. Introduction

High throughput experimentation (HTE) of materials is developing as an efficient method to accelerate the discovery of new compounds and to identify the best candidates related to a specific functional property. This approach combines the preparation of a large number of samples with varying compositions (i.e. material libraries) by combinatorial synthesis, followed by their fast and automated physical-chemical and functional characterization, and usefully completed by advanced processing of the generated data sets [1–3]. It may bring beyond traditional trial-and-error experiments for the discovery of breakthrough materials and contribute to a deeper understanding of underlying structure-composition-property relationships.

Magnetron sputtering, which is a widely used process for the deposition of inorganic thin films, can be easily adapted to perform combinatorial syntheses of a large variety of materials comprising metals, ceramics, glasses and combinations of the latter. The simplest method consists in carrying out co-deposition of chemical species originating from multiple targets located around a substrate, which mix at the surface of the latter and generate composition gradients. As a result, a material library can be generated on a single substrate in a single experiment. The counterpart of this simplicity is that the chemical composition and the thickness of the film at each location on the substrate cannot be precisely monitored and has to be analysed a posteriori, in addition to other properties. To implement the HTE approach, a fast and spatially resolved method for quantitative chemical analysis is required. Since its first application in the ‘70s [4], HTE has been carried out for the identification of new complex materials among metallic alloys [5,6], oxides [7,8], nitrides [9,10], borides [11], phosphides [12], sulfides [13] for enhancing various functional properties. Energy Dispersive X-ray spectroscopy (EDX), X-Ray Fluorescence spectrometry (XRF), were extensively used for their chemical analysis. Field Emission Electron Probe Micro-Analyser (FE-EPMA), Auger Nanoprobe, X-ray Photoelectron Spectroscopy (XPS) and Rutherford Backscattering Spectrometry (RBS) were eventually used as complementary methods, but it is obvious that these techniques are difficult to conciliate with a high throughput approach.

In the case of lithium battery materials, HTE approach using

---

* Corresponding author at: Univ. Bordeaux, CNRS, Bordeaux INP, ICMCB, UMR 5026, F-33600 Pessac, France.
** Corresponding author.
E-mail addresses: bruno.bousquet@u-bordeaux.fr (B. Bousquet), frederic.lecras@cea.fr (F. Le Cras).

https://doi.org/10.1016/j.sab.2024.106906
Received 21 December 2023; Received in revised form 20 March 2024; Accepted 23 March 2024

combinatorial synthesis by sputtering can be applied to assess the properties of electrodes, solid electrolytes and couples made of thereof. In that respect, extensive and pioneering investigations were conducted on Li-free compounds as negative electrode materials [14], using a specific sequential deposition method [15]. Nevertheless, most of battery materials contain lithium as a major element. Since the latter is not detectable by EDX and XRF, the challenge for the development of such HTE on lithium battery materials is to develop a technique capable of providing quantitative spatially-resolved elemental composition, for lithium and other light elements. In such context, S. Borhani-Haghighi et al. [16] were the first to report quantitative chemical mapping for all elements (including lithium) in the Li-Co-Mn-O positive electrode system. To achieve this goal, global fitting of data from EDX, RBS and DIGE measurements was applied.

However, none of these methods is able to perform true high-throughput chemical analysis of lithium in combinatorial thin-film libraries, as the latter requires the following features at the same time:

(i) Quantitative analysis of lithium (and possibly other light elements)
(ii) Spatially resolved sampling & analysis (< 1 mm^2)
(iii) Ability to scan large substrates (typically 4″ wafers)
(iv) High sensitivity to detect and quantify small amount of analyte
(v) Fast analysis to be considered as a true high-throughput method

Laser-Induced Breakdown Spectroscopy (LIBS), especially when operated for mapping purpose, is ideal to meet all the expectations of this list. In LIBS, a high power pulsed laser beam is focused onto the sample surface. The resulting irradiance induces the ablation and vaporization of a small amount of matter which forms a transient plasma of small dimension, containing the chemical species originally making the chemical composition of the sample. When this plasma expands and cools down, it emits a radiation that is analysed by an optical spectrometer in a spectral range from UV to near IR. The LIBS spectrum is composed of atomic emission lines well-documented in spectral databases, which intensity levels vary with the amount of related species. LIBS can be operated in a single-shot mode so that multi-elemental mapping can be performed in a relatively short time, defined by the acquisition frequency. These last years, LIBS imaging has been successfully applied to various fields such as geochemistry [17–19], biomedical [20], archaeology [21–23] and industry [24,25]. In a context of a soaring lithium battery market, LIBS has been used for a variety purposes from characterizing mineral ores [17,26] to chemical mapping of lithium-based battery components [27–32] and monitoring recycling processes [24,33].

The aim of this work is to evaluate the capability of LIBS imaging as a possible method for analysing the elemental composition of lithium-based thin films. To this end, the lithium phosphorus oxide ($Li_xP_yO_z$) system was chosen as a case study. Indeed, the oxynitride form (LiPON) is widely used in all-solid-state thin-film microbatteries [34,35], and recently gained a new interest as protective interlayer in bulk all-solid-state lithium batteries [36,37]. LiPO(N) materials, prepared by reactive sputtering of Li_3PO_4 in pure argon or reactive nitrogen plasma, are amorphous, glassy solid Li^+ ionic conductors. Ion transport in these materials is governed by their local structure and the nature of the [PO_aN_b] building blocks [38,39], which in turn is influenced by their overall chemical composition. Investigating of a wide range of compositions would therefore contribute to confirm the present understanding of the composition-structure-ionic transport relationships or to unveil new correlations.

2. Materials and methods

2.1. Thin films synthesis

Lithium phosphorus oxide ($Li_xP_yO_z$) was deposited on 4″ diameter silicon single-crystal wafers (100 orientation, boron doped) by magnetron sputtering (Plassys Bestek) from a 2″ diameter Li_3PO_4 target (Neyco, 99.9%). The wafer substrate was positioned horizontally 107 mm above the target, and its centre was offset by 25 mm from that of the target (Fig. 1(a)), to generate a film thickness gradient along the wafer surface, as observed in Fig. 1(b).

Prior to material deposition, the sputtering chamber was evacuated to a pressure of $6.5 \cdot 10^{-5}$ Pa. Pre-sputtering of the target was conducted at first during 45 min before initiating deposition on the substrate. Sputtering conditions were set at an incident power of 3.65 W.cm^{-2} and pure argon pressure of 1 Pa. Deposition was performed through a shadow mask so that the LiPO films are deposited as an array of 3 × 3 mm squares on the wafer (Fig. 1(b)).

Three wafers were prepared in a row according to this protocol, each one corresponding to a given deposition time. Deposition times of 0.5, 2 and 6 h were chosen to obtain sample thicknesses ranging from 10 to 700 nm, the latter depending on the process duration and the distance between the target and the location of the sample at the surface of the substrate. The different film thicknesses are easily visible to the naked eye, as they induce a variety of colours when exposed to white light (Fig. 1(b)) due to interference.

2.2. Films characterization

2.2.1. Film thickness

Film thicknesses were measured using an automated stylus profilometer (Bruker, DektakXT) and a 12.5 μm tip radius. Its precision is up to 5 nm. Tip force was set at 1 mg. Height profiles were measured over 4 mm sections for each square sample with an excellent repeatability. In addition, three-dimensional measurements on 4 × 4 mm^2 areas were carried out to check thickness homogeneity over the entire surface of each square sample.

2.2.2. Laser induced breakdown spectroscopy

The LIBS setup used to characterize LiPO films has been described previously [40]. Briefly, a 1064 nm, 8 ns, 1.0 mJ, 100 Hz laser beam is focused onto the sample surface at a spot size of about 10 μm in diameter, and a single shot is delivered per location. The laser cross section holds a quasi-Gaussian shape $M^2 \approx 1$ (Centurion GRM, Lumibird). A focusing lens of x15 is used within the setup. Measurements are done under air, and a continuous argon flow (1 l.min^{-1}) is directed towards the ablation zone. Argon is used in order to enhance plasma emissivity and reduced self-absorption [41,42]. Sample surface is scanned using an XY-translation stage. Analysis of 4 × 4 mm^2 square samples was conducted by firing 180 × 100 shots spaced 35 μm apart. 40 samples out of the 76 available on each wafer were analysed that way for 2 h and 6 h depositions, and 20 samples were analysed for the 0.5 h deposition. Three different Czerny-Turner spectrometers coupled to ICCD cameras enabled to detect and analyse the emission lines related to Li, P, O, Si and H. Their respective features are provided as Supplementary Information. Finally, data were extracted using a process already described [43]. To guarantee the best conditions of homogeneity and representativeness, restricted sub-areas of 50 × 50 ablation craters within each sample are considered. Those areas are selected because of their homogeneous thickness and homogeneity. Thus, a mean value of the area of each analyte peak is calculated.

2.2.3. Inductive coupled plasma - optical emission spectroscopy

Inductively Coupled Plasma – Optical Emission Spectroscopy (ICP-OES) was used (Agilent ICP/OES 5800 DV) to get the Li and P contents of the LiPO thin films. A specific sputter deposition was conducted to prepare samples to be analysed by ICP-OES. For this purpose, film deposition was performed during 6 h on polytetrafluoroethylene (PTFE) disks of 15 mm in diameter and 0.5 mm thick placed on the wafer at locations matching the positions of square samples generated during the regular deposition process, and attached to it using Kapton® adhesive

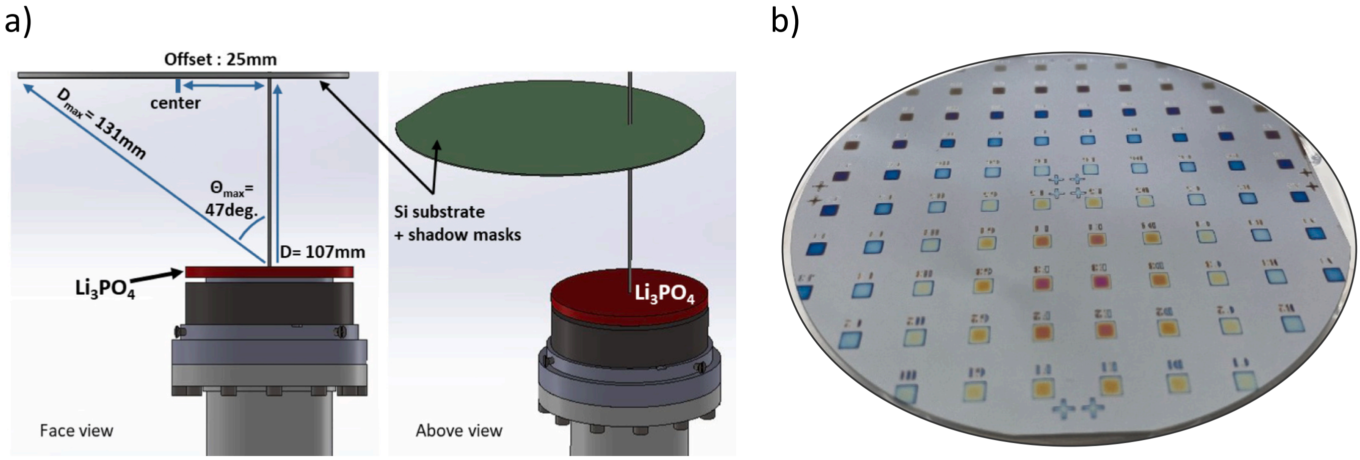

Fig. 1. (a) Relative positions of target (Li_3PO_4; red) and substrate (Si wafer; green) during magnetron sputtering; (b) Photograph of the material library generated on the silicon wafer by deposition through a shadow mask. The variation in colour, generated by interference of white light waves, highlights the thickness gradient. (For interpretation of the references to colour in this figure legend, the reader is referred to the web version of this article.)

tape. Sputtering parameters were kept unchanged relative to the other deposition experiments. After deposition, each PTFE disk was detached from the wafer and immersed in a solution of 2.5 ml HCl + 2.5 ml HNO_3, made up to 50 ml with deionized water, to dissolve the LiPO film. Finally, a small quantity of each solution was analysed by ICP-OES and this analysis was repeated five times for each solution, i.e. for each disk. These ICP-OES analyses were based on the Li emission line at 670.79 nm and the P emission line at 253.56 nm.

2.2.4. Scanning electron microscopy

Laser damage induced on the film/substrate during LIBS characterization was investigated using In-lens Scanning Electron Microscopy (In-lens SEM) (Zeiss, Sigma 500) consisting in a 10 kV electron beam at a working distance of 5.0 mm. Top and front views together as well as cross-sections were recorded for several ablation craters.

3. Results

3.1. Mapping of film thicknesses

Deposition through a shadow mask allows the film to be discretized into 76 square samples and generates multiple steps between masked and unmasked areas needed to determine the thickness of each sample by stylus profilometry. Fig. 2(a) shows an example of 3D reconstructed view of a square sample of film generated from series of thickness profiles, which highlights a very satisfying homogeneity and drives to consider single central cross-sections (Fig. 2(b)) as representative of the whole film.

Therefore, the thickness of each sample was determined by measuring six profiles, i.e. three along the X axis and three along the Y axis, across the middle of the pattern and at distances of +/− 0.5 mm from the centre. Fig. 3 displays the mean value obtained across each sample and the standard deviation for 2-h and 6-h depositions, and confirms the presence of a gradient due to different sample-to-target distances. The thicknesses of the samples varied from 70 to 700 nm (Fig. 3(a)) for a 6-h deposition, and from 15 to 250 nm for a 2-h deposition (Fig. 3(b)). In the case of the 0.5 h deposition, it was difficult to accurately measure the thicknesses of these samples, most of them were well below 50 nm, which is close to the detection limit of the profilometer. We therefore considered estimating them indirectly by dividing by 4 the corresponding values measured during the 2 h deposition, assuming a constant deposition rate.

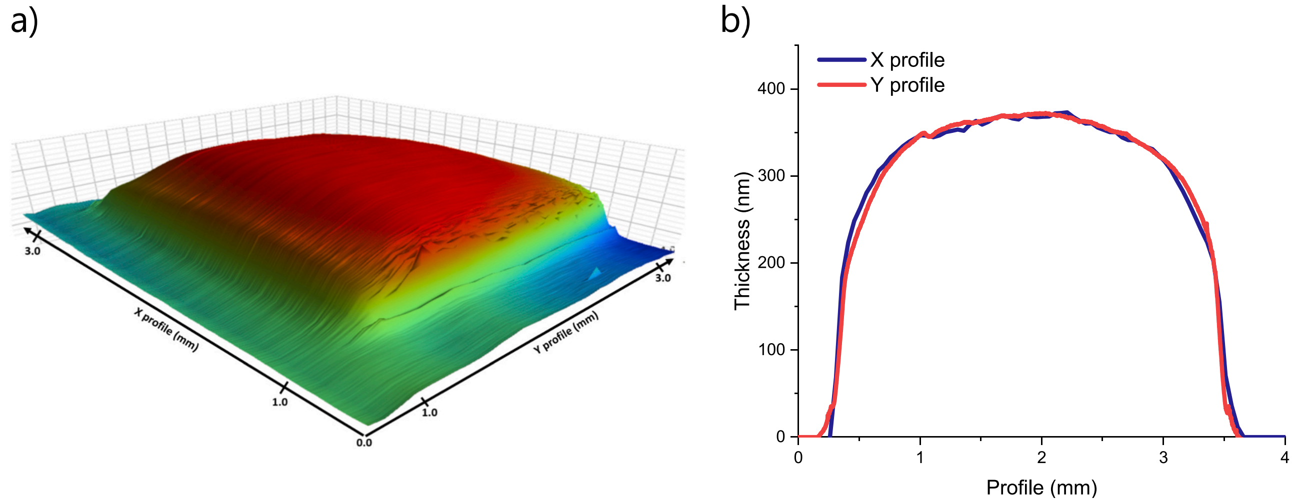

Fig. 2. (a) Example of 3D thickness profile of LiPO thin film (a) colour-coded from blue for depth equal to zero to red for maximum depth, and (b) central cross-section profiles along the orthogonal (X, Y) directions of the physical mask used to delimit the deposition area. (For interpretation of the references to colour in this figure legend, the reader is referred to the web version of this article.)

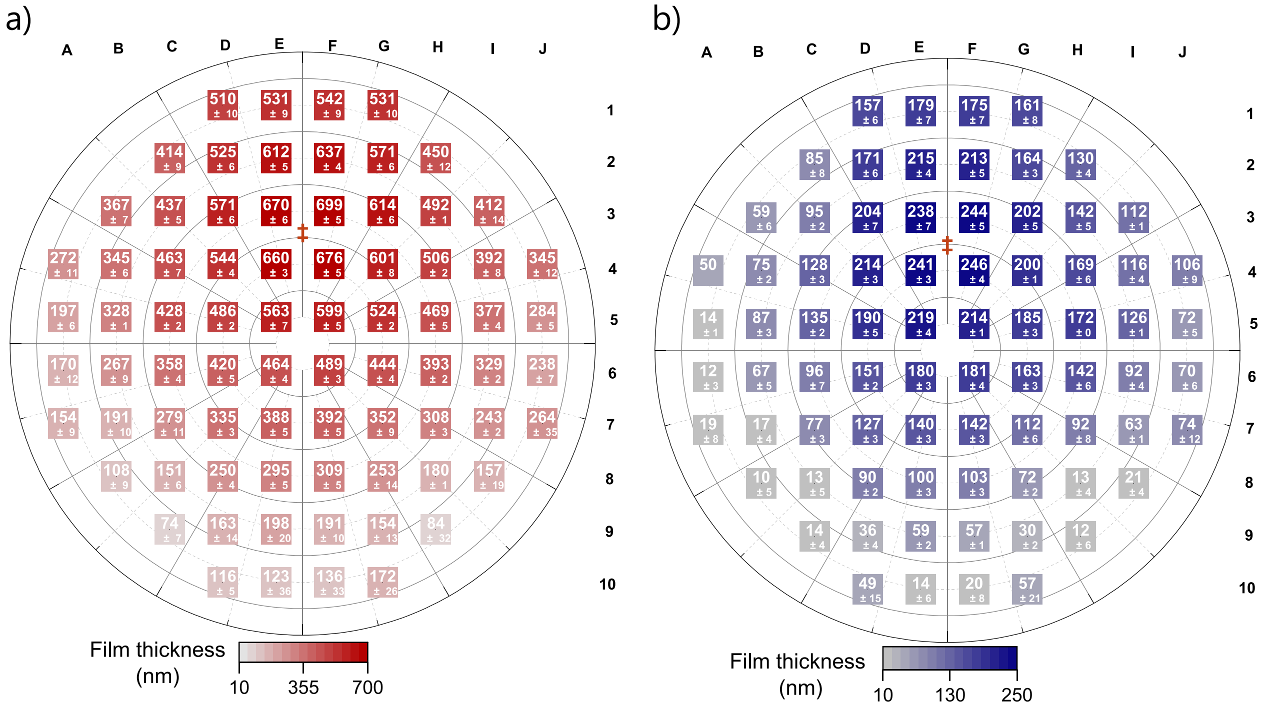

a)

	A	B	C	D	E	F	G	H	I	J
1				510 ± 10	531 ± 9	542 ± 9	531 ± 10			
2			414 ± 9	525 ± 6	612 ± 5	637 ± 4	571 ± 6	450 ± 12		
3		367 ± 7	437 ± 5	571 ± 6	670 ± 6	699 ± 5	614 ± 6	492 ± 1	412 ± 14	
4	272 ± 11	345 ± 6	463 ± 7	544 ± 4	660 ± 3	676 ± 5	601 ± 8	506 ± 2	392 ± 8	345 ± 12
5	197 ± 6	328 ± 1	428 ± 2	486 ± 2	563 ± 7	599 ± 5	524 ± 2	469 ± 5	377 ± 4	284 ± 5
6	170 ± 12	267 ± 9	358 ± 4	420 ± 5	464 ± 4	489 ± 3	444 ± 4	393 ± 2	329 ± 2	238 ± 7
7	154 ± 9	191 ± 10	279 ± 11	335 ± 3	388 ± 5	392 ± 5	352 ± 9	308 ± 3	243 ± 2	264 ± 35
8		108 ± 9	151 ± 6	250 ± 4	295 ± 5	309 ± 5	253 ± 14	180 ± 1	157 ± 19	
9			74 ± 7	163 ± 14	198 ± 20	191 ± 10	154 ± 13	84 ± 32		
10				116 ± 5	123 ± 36	136 ± 33	172 ± 26			

b)

	A	B	C	D	E	F	G	H	I	J
1				157 ± 6	179 ± 7	175 ± 7	161 ± 8			
2			85 ± 8	171 ± 6	215 ± 4	213 ± 5	164 ± 3	130 ± 4		
3		59 ± 6	95 ± 2	204 ± 7	238 ± 7	244 ± 5	202 ± 5	142 ± 5	112 ± 1	
4	50	75 ± 2	128 ± 3	214 ± 3	241 ± 3	246 ± 4	200 ± 1	169 ± 6	116 ± 4	106 ± 9
5	14 ± 1	87 ± 3	135 ± 2	190 ± 5	219 ± 4	214 ± 1	185 ± 3	172 ± 0	126 ± 1	72 ± 5
6	12 ± 3	67 ± 5	96 ± 7	151 ± 2	180 ± 3	181 ± 4	163 ± 3	142 ± 6	92 ± 4	70 ± 6
7	19 ± 8	17 ± 4	77 ± 3	127 ± 3	140 ± 3	142 ± 3	112 ± 6	92 ± 8	63 ± 1	74 ± 12
8		10 ± 5	13 ± 5	90 ± 2	100 ± 3	103 ± 3	72 ± 2	13 ± 4	21 ± 4	
9			14 ± 4	36 ± 4	59 ± 2	57 ± 1	30 ± 2	12 ± 6		
10				49 ± 15	14 ± 6	20 ± 8	57 ± 21			

Fig. 3. Thickness maps of LiPO samples, obtained by stylus profilometry on 4″ wafers, for two deposition durations (a) 6 h, in red and (b) 2 h, in blue. Mean values and standard deviations are provided for each square sample. The double-barred cross (‡) represents a projection of the target center. (For interpretation of the references to colour in this figure legend, the reader is referred to the web version of this article.)

3.2. *Ablation craters and laser-induced damages*

A selection of craters was imaged by In-lens SEM after LIBS analysis to examine the impact of single and multiple laser ablations on the surface of the coated/un-coated wafer. Fig. 4(a) displays a relatively wide top-view showing that the ablation craters are regularly spaced, with no overlap between them, and that there is no evidence of dramatic damage such as cracks or large-scale material alteration or destruction. This indicates that the experimental set-up is well controlled and that the laser fluence selected for this mapping mitigates laser-induced damages. Fig. 4(b) shows a top view of one typical ablation crater of the series displayed in Fig. 4(a) and (c) a related side view. Both reveal that the typical ablation craters are approximatively conical, with a maximum depth of about 7 ± 1 μm and a diameter of around 12 ± 2 μm. Moreover, various types of droplets are clearly visible in Fig. 4(b), probably resulting from redeposition of molten materials after plasma expansion and cooling. Our observations have shown that the diameter and the depth do not vary significantly from one crater to another, so that Fig. 4(b) and (c) can be considered representative of the whole set.

Direct observation of the laser ablation craters demonstrates that the ablation depth is far greater than the thickness of the films deposited on the silicon wafer, which is always <700 nm. This means that silicon is always ablated, whatever the film thickness. It is also worth mentioning that the craters diameter and depth values stay very similar whatever the laser spot hits a surface of bare silicon wafer or the film of LiPO deposited on it. Thus, no significant difference in laser ablation was observed with or without the presence of thin film at the surface of the silicon wafer.

These observations show that the depth of ablation is always be much greater than the thickness of the LiPO samples, which remains between 50 and 700 nm. Consequently, the detection of silicon can be expected in all spectra, since the laser-induced plasma is expected to be mainly composed of silicon species. If we consider that the LiPO and Si materials are organized in two distinct strata, we can assume as the first approach that the LIBS signal linked to Si should decrease continuously as the film thickness increases, while the signals linked to the Li, P and O that make up the deposited film should increase continuously. To support this intuitive view with a simplistic model, let us consider that the ablation crater can be described by a cone of diameter 2R and depth d, with e the film thickness (supposed to be always smaller than d). Then, we can easily write:

- $V_{total} = \frac{1}{3}\pi R^2 d$, the total ablation volume;
- $V_{substrate} = V_{total}\left(1 - \frac{e}{d}\right)^3$, the fraction of this volume containing only the substrate;
- $V_{film} = V_{total} - V_{substrate}$ the fraction of this volume containing only the film

When $\frac{e}{d} \ll 1$, which is the case here (e varies between 0.05 and 0.7 μm, while d is equal to 7 μm), approximation of the equations by a limited development leads to $V_{film} = V_{total} \times 3 \bullet \frac{e}{d}$ and $V_{substrate} = V_{total} \times \left(1 - 3 \bullet \frac{e}{d}\right)$. Under these conditions, we can consider that $V_{substrate}$ is linearly decreasing for increasing film thickness values, whereas V_{film} is linearly increasing, starting from zero. The cubic trends of $V_{substrate}$ and V_{film} could be observed only for much thicker films. Finally, considering that the LIBS signal is proportional to the number of corresponding species present in the plasma, and then, assuming a stoichiometric ablation of the sample, we can conclude that the LIBS signal is proportional to the ablated volume of material containing this species. Consequently, we expect to measure experimentally a linear decrease in the LIBS signal of Si (silicon wafer substrate), and a linear increase (from zero) in the LIBS signals of Li, P, O (LiPO thin film).

3.3. *Mapping of Li/P atomic ratio by ICP-OES*

ICP-OES analyses were performed to determine the actual Li/P atomic ratio in the LiPO film samples, and to assess its distribution, if not its stability, across the entire wafer surface. Fig. 5 shows the layout of samples prepared by 6-h sputtering from a Li_3PO_4 target, in which grey circles indicate the exact locations of the PTFE disks that were used to perform the ICP-OES analyses. Each disk corresponds to a given film

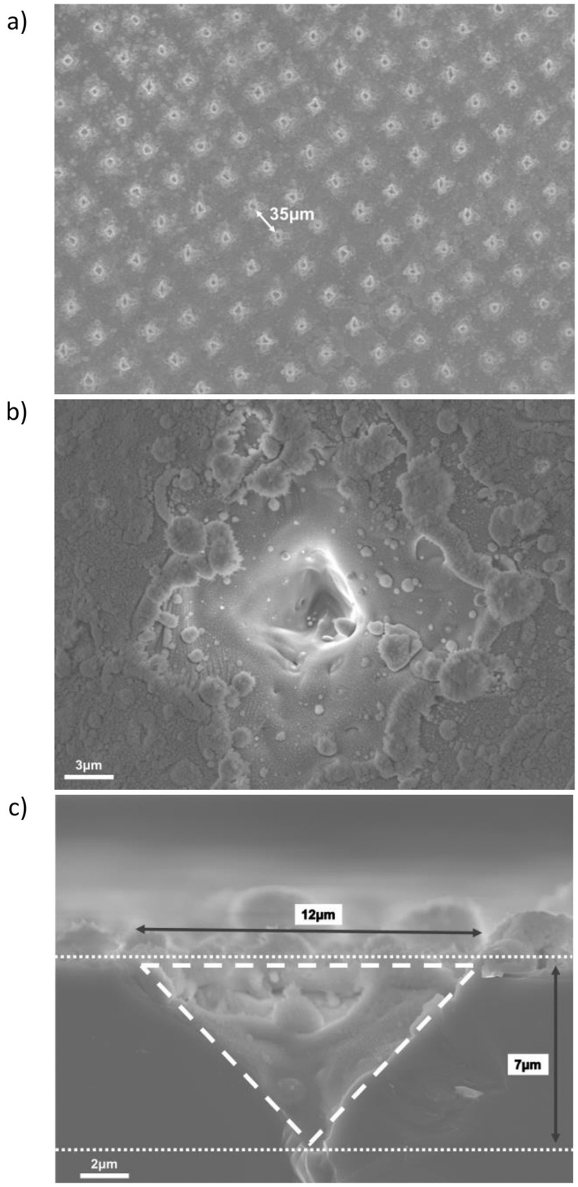

Fig. 4. SEM images of a coated silicon wafer after LIBS analyses: (a) top view showing a series of laser ablation craters with a spacing of 35 µm at the surface of the wafer, (b) top view centred on one single ablation crater, (c) cross-section view of an ablation crater.

thickness value ranging from 100 to 700 nm (see Fig. 3(b)).

The Li/P atomic ratio value of 2.3 on average indicates that the original stoichiometry giving a ratio equal to 3 has not been preserved. The interest for calibration of LIBS measurements lies in the fact that the measured values of this atomic ratio is almost constant over the entire substrate and independent of film thickness. Consequently, if relative variations in intensity were observed on LIBS spectra between different elements, they will depend exclusively on variations in film thickness and not on a change in composition.

3.4. LIBS analyses: towards quantification

3.4.1. General considerations

Typical single-shot LIBS spectra of LiPO thin film deposited on silicon wafer are displayed in Fig. 6, as obtained by the three spectrometers implemented in our setup. Si, P, Li, O, Ar and H atomic emission lines are detected. More precisely, LIBS spectra exhibit intense lines as the Si I lines at 212.41 and 221.69 nm, the P I lines at 214.91 nm, the Li I lines at 413.00, 460.29, 610.35 and 670.79 nm, and the H I line at 656.10 nm. Interestingly, the two lithium lines at 610.35 and 670.79 nm are detected even at the lowest film thickness values.

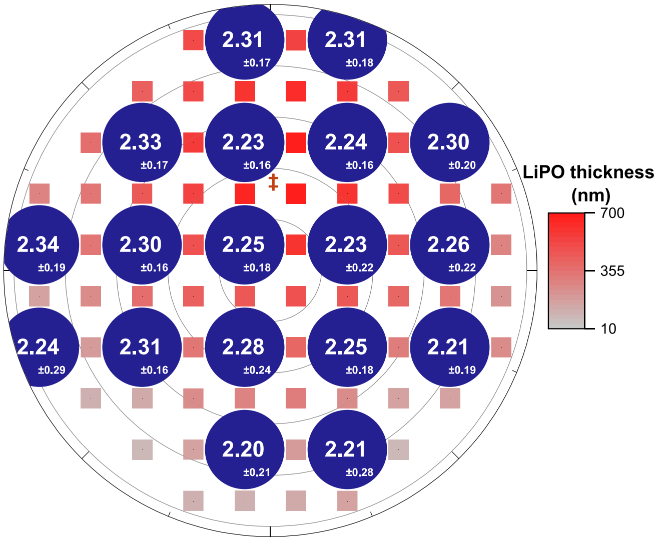

Fig. 5. Li/P atomic ratios determined by ICP-OES measurements on samples prepared by 6-h sputtering from a Li_3PO_4 target. The uncertainty corresponds to the standard deviation of the results of 5 analyses performed on each sample. Colour code indicates film thickness values. The double-barred cross (‡) represents a projection of the target center.

Since the prerequisite for quantitative analysis is to verify the stability of the LIBS signal, LIBS analyses were carried out on a bare silicon wafer as a reference sample, probing six zones of 3.5 × 2.1 mm^2, spaced 2 cm apart, and recording 6000 spectra per zone. From these measurements, the average LIBS signal for each area and the RSD value derived from this series of six values were calculated. In this case, the Si I emission line at 212.41 nm was selected and a RSD value $<5\%$ was obtained, highlighting the good stability of our experimental conditions. This result was considered as a pass to perform further quantitative analysis of the deposited films.

3.4.2. LIBS characterization of thin film libraries

On the basis of this result, LIBS measurements were then carried out on three series LiPO samples prepared on separate wafers and corresponding to three different deposition durations. Results corresponding to analysis of lithium emission lines are provided at first in Fig. 7, which displays the evolution of the LIBS signals of lithium (460.29, 610.35 and 670.79 nm) as a function of the film thickness. As a reminder, each dot on the plots corresponds to a square sample present on a wafer and to a mean value of about 50 × 50 spectra. The experimental data confirm the linear trend that was expected, but the latter is only valid when two separate thickness ranges are considered: from 700 nm to 50 nm with a limited slope, and below 50 nm, where the Li signals vary strongly with thickness. Besides, a greater dispersion of the data is observed for the 460.29 nm emission line compared to the other two. This may suggest that slight variations in experimental conditions could have a more marked influence at this wavelength, for reasons that need to be investigated.

However, the most intriguing point, apart from the presence of two quasi-linear domains, is the fact that all three plots show that the signal corresponding to a film thickness close to zero is significantly different from zero. This result clearly suggests that lithium atoms have penetrated inside the silicon wafer. Lithium penetration inside a silicon single-crystal is likely and well documented in the framework of lithium contamination, especially in microelectronics [44,45]. However, in the case of magnetron sputtering at ambient temperature, the diffusion

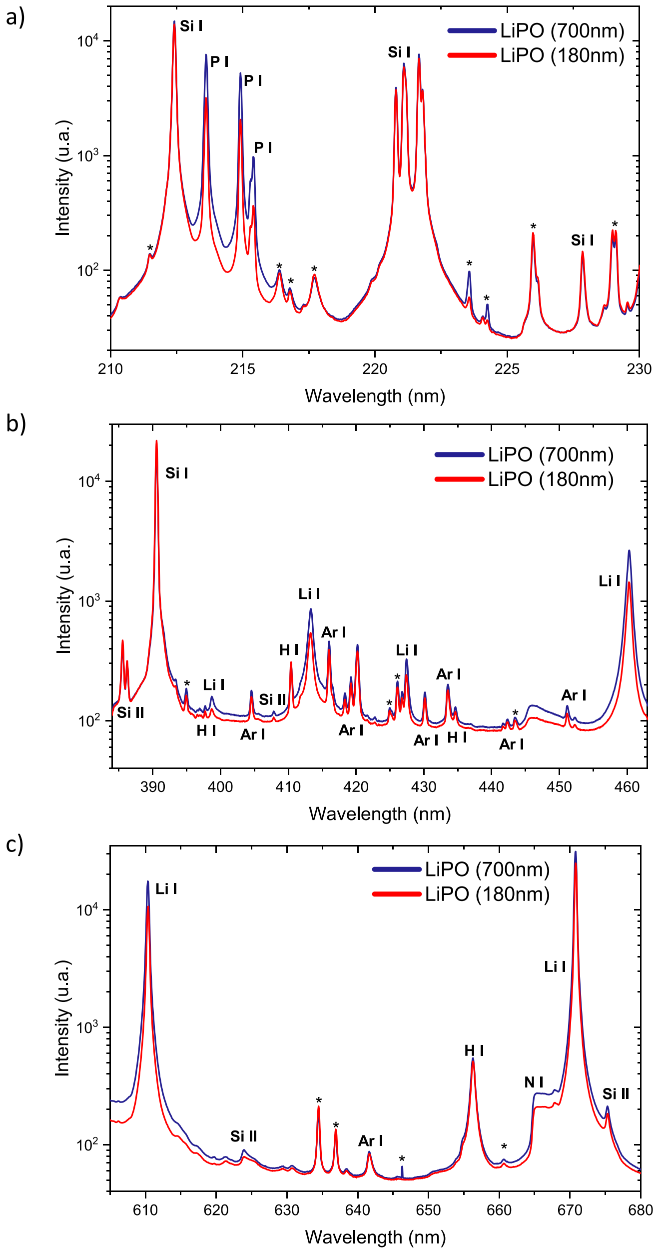

Fig. 6. Typical single-shot LIBS spectra of a LiPO thin film deposited on a silicon wafer. The three discontinuous (a), (b) and (c) spectral ranges, respectively related to three spectrometers of our setup, are the result of the same single-shot laser ablation. * represents non-assigned peaks.

depth of lithium (in the form of neutral atoms) inside silicon should be limited to the sub-micron range. Moreover, it is interesting to note that, for the 100–200 nm thickness range, the LIBS signals measured for films deposited during 2 and 6 h are very similar (red and blue dots overlap). This result indicates that there is no significant difference of lithium penetration between these two sputtering times. However, at some point, for very short sputtering times, the amount of lithium that penetrates inside the substrate should increase with sputtering duration.

Turning now to phosphorus, Fig. 8 shows the evolution of the LIBS signal of phosphorus at 214.91 nm as a function of the LiPO film thickness. The trend is almost linear but a specific regime at small thickness values is very likely to be present, as it was the case for lithium. We can therefore conclude that phosphorus also penetrates the silicon substrate. Such a phosphorus penetration mechanism has been reported by diffusion at high temperature [46,47], but the penetration depth in the context of sputtering is expected to be very shallow, namely at the nanometre scale.

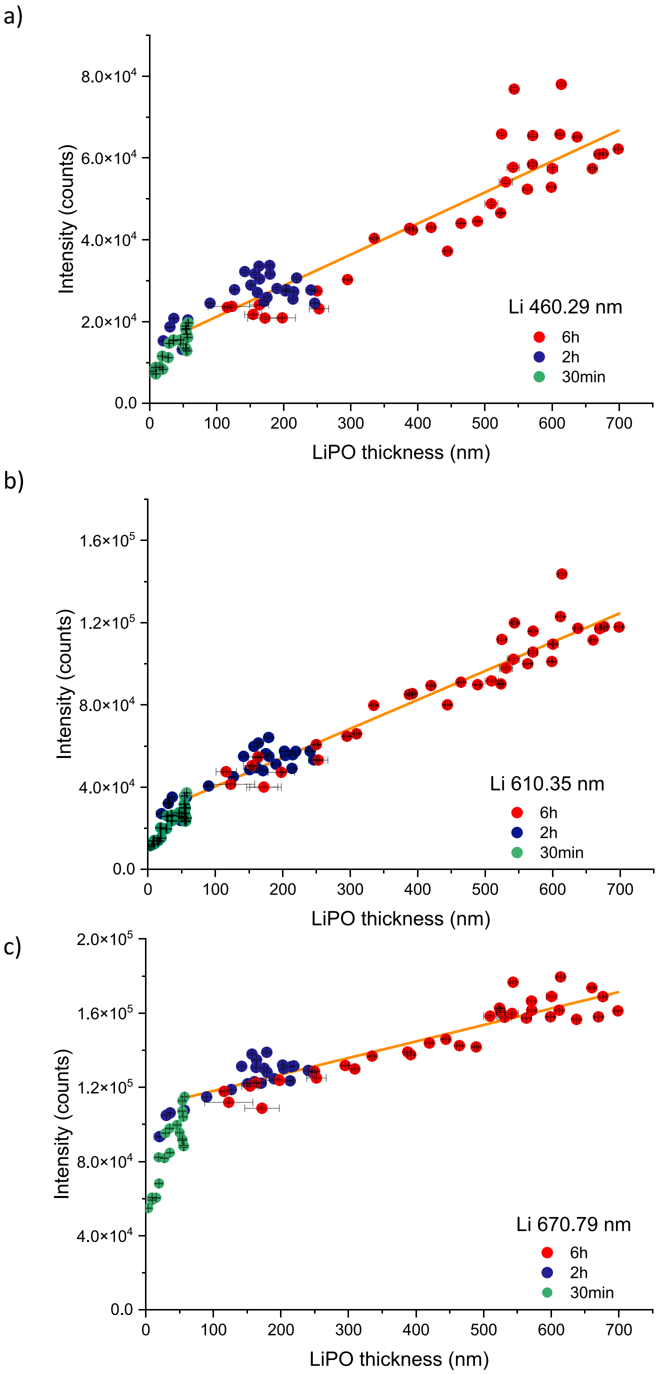

Fig. 7. Evolution of the LIBS signal for Li I at 460.29 nm (a), 610.35 nm (b) and 670.79 nm (c) as a function of the LiPO film thickness. Red, blue and green markers indicate sputtering time of 6 h, 2 h and 0.5 h, respectively. (For interpretation of the references to colour in this figure legend, the reader is referred to the web version of this article.)

Finally, LIBS analyses on phosphorus and lithium show both linear trends with the quantity of deposited material in the 50–700 nm film thickness range (which corresponds to the quantification of ca. 2–20 pg of Li). This is an outstanding result driving to conclude that LIBS is perfectly adapted to perform quantitative analysis of thin films within the framework of HTE approach.

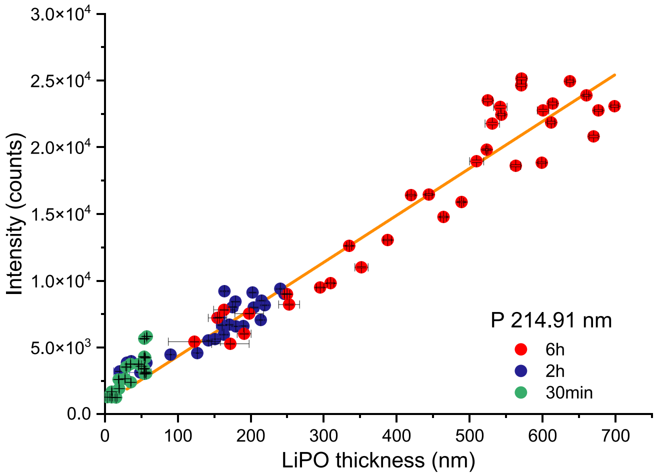

Fig. 8. Evolution of the LIBS signal for P I at 214.91 nm as a function of the LiPO film thickness.

3.4.3. *Species penetration inside the substrate during sputtering*

Our results clearly highlight that there is a specific regime related to very small thicknesses of thin deposited on the silicon single-crystal wafers that should be understood to fully validate the method. At this stage, these results suggest that both Li and P can penetrate into the silicon crystal.

In order to check whether the introduction of Li and P species in the Si substrate could possibly take place during the steps preceding the actual sputter deposition, a series of 3 wafers were analysed by LIBS. This series consisted of a pristine silicon wafer, never introduced into the sputtering chamber, and considered as the reference sample; a silicon wafer simply stored for 45 min inside the sputtering chamber; and a silicon wafer introduced inside the sputtering chamber and exposed to a 30 min pre-sputtering process, meaning that a closed shutter is interposed between the Li$_3$PO$_4$ target and the wafer during the process. These three samples thus cover the entire sample processing chronology prior to the deposition step. In each case, LIBS signals of phosphorus at 214.91 nm and lithium at 670.79 nm were examined. Indeed, while the Li I emission line at 670.79 nm is often discarded due to strong self-absorption and even self-inversion effects in many cases, it becomes the best choice to answer the question of the limit of quantification.

With regard to phosphorus in the first place, the intensity of P I 214.91 nm was found to remain almost constant around 125–150 counts (which actually corresponds to an absence of signal) under the three conditions of preparation. This indicates that none of preparation step contribute to a contamination of the substrate by phosphorus. Consequently, the intercept point at an intensity of around 1000 counts for zero thickness visible in Fig. 8 can only be explained by the incorporation of P into the Si substrate during the deposition process, or possibly afterwards. Therefore, either P is entered in the Si single-crystal as individual neutral atoms originating directly from the target, or was able to diffuse from the LiPO film. In both cases, the depth of diffusion in the substrate is certainly much less than the depth of the laser ablation crater, which means that the whole amount of phosphorus that has reached the substrate is always taken into account during LIBS analysis, whatever the film thickness in the range 0–700 nm.

Considering lithium, the LIBS signal of Li I 670.79 nm was recorded at around 10 counts for the reference silicon wafer. This value rises to 40 counts for the wafer after 45 min storage in the chamber, and finally to 260 counts (SNR ≈ 1.7) after 30 min pre-sputtering. Considering the LIBS signals obtained after sputtering, the intercept at 50,000 counts observed in Fig. 7c is extremely high compared to the levels measured prior the sputtering step. This result is also a striking evidence that a significant amount of Li was able to incorporate into the Si wafer during the deposition process. Furthermore, the extrapolated value of the film thickness that would correspond to a zero signal is significantly higher in absolute value for lithium (Fig. 7b) than for phosphorus (Fig. 8), which seems to show that the proportion of Li lost in the substrate is greater than that of phosphorus, and which could be consistent with the higher diffusivity of Li.

Additional experiments based on shorter sputtering times of only 2 to 20 min were performed to specifically investigate the hypothetical thickness range of 0 to 50 nm, which is not measurable by stylus profilometry. This allowed us to confirm that the LIBS signal is indeed proportional to the amount of species that have reached the substrate (whether the species have penetrated the substrate or have been deposited on its surface) (Fig. 9). This additional result suggests that the incorporation of species into the silicon crystal takes place mainly during the early stages of deposition, when the Si surface is not yet modified by the arrival of elements from the target or already covered by a LiPO film, and therefore the single crystal surface is still relatively exposed.

LiPO deposition rate measured in steady state conditions (i.e. long deposition times) being of approx. 115–120 nm.h^{-1} in our experimental conditions, 2 min deposition corresponds to the deposition of 4 nm of LiPO. Assuming a density of around 2.4 g.cm^{-3}, which lies between the densities of crystalline Li$_4$P$_2$O$_7$ and Li$_3$PO$_4$ materials, and considering an ablated area of 12 μm in diameter, this means that a maximum of around 0.15 pg of Li and 0.34 pg of P were ablated in single laser shot (the detailed calculation is provided as Supplementary Information). That generates respective signal intensities of around 12,890 counts for Li I 670.79 nm (SNR =160) and 106 counts for P I 213.62 nm (SNR =1.2). This phosphorus line was chosen because it exhibits a sharp profile, and is highly distinguishable compared to Si pristine spectrum (Fig. A & B in *SI*). This result is therefore a powerful demonstration of the high sensitivity of the technique and its value for thin-film analysis.

3.5. *Comparison LIBS/ICP-OES*

ICP-OES data giving Li/P concentration ratios have already been presented (Fig. 5). Here, the ICP-OES data are examined directly through the intensity signal of each emission lines, namely Li I 670.79 nm and P I 253.51 nm. In Fig. 9, ICP-OES and LIBS signals for lithium and phosphorus emission lines are displayed as a function of the film thickness. Fig. 10 reveals that the two trends (ICP-OES and LIBS) superimpose well. It means that the penetration of Li and P inside the silicon crystal has negligible influence on the LIBS signal compared to the amount of LiPO thin film deposited onto the surface after 6 h deposition. Finally, this result clearly demonstrates the ability of LIBS to perform quantitative analysis of thin films.

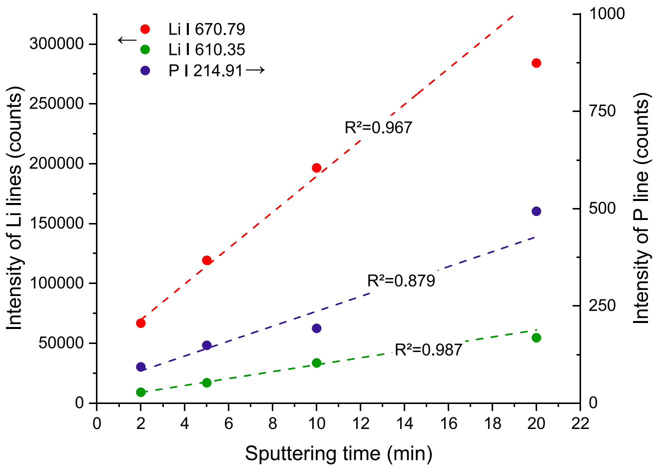

Fig. 9. Evolution of the Li I 670.79 nm, Li I 610.35 nm and P I 214.91 line intensities (LIBS) as a function of deposition time, for a deposition rate of 120 nm.h^{-1}.

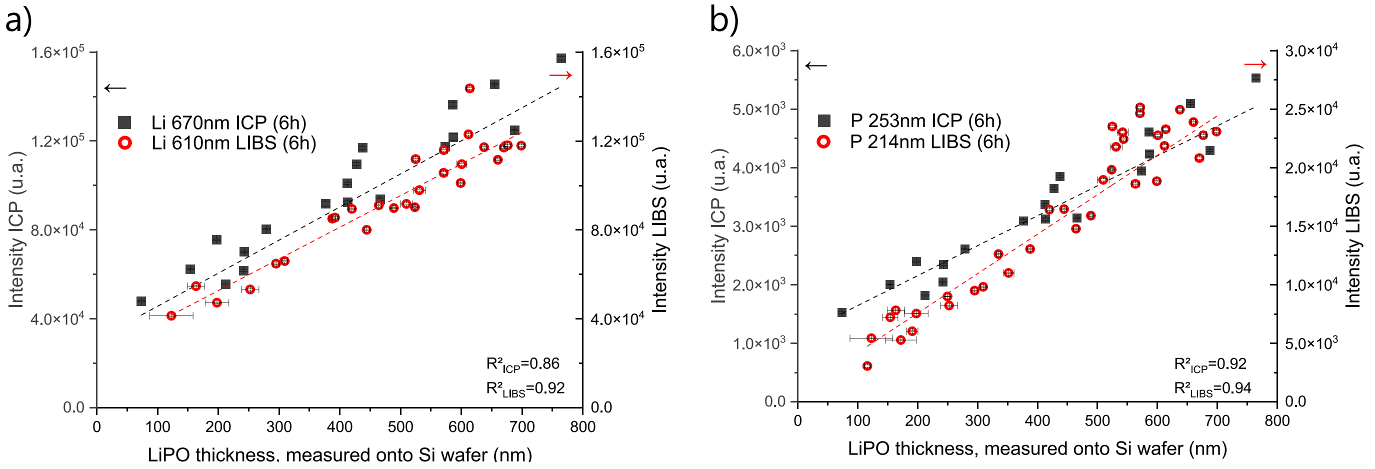

Fig. 10. ICP-OES signal (left axis) and LIBS signal (right axis) for lithium (a) and phosphorus (b) as a function of the film thickness (obtained after 6 h deposition).

4. Conclusion

In this work, Laser-Induced Breakdown Spectroscopy was assessed as a quantitative elemental analysis technique and for its compatibility with the High-Throughput Experimentation approach based on combinatorial synthesis of thin film materials. Application of this method in the particular case of lithium battery materials was carried out through the case study of amorphous lithium phosphate (LiPO) thin films. Films with thickness ranging from 10 to 700 nm, were prepared by magnetron sputtering on 4″ silicon wafer as thin film material libraries composed of 76 samples. Chemical and dimensional mapping were conducted of the entire wafer substrates respectively by LIBS, ICP-OES and stylus profilometry. ICP-OES has confirmed the good homogeneity of the Li/P atomic ratio equal to ca. 2.3 over the entire substrate. LIBS mapping, performed with a 35 μm spacing, allowed the acquisition of spectral images for several emission lines of lithium and phosphorus (film) and silicon (substrate). Laser-ablation craters were found to be very similar across the wafer with typical depth of 7 μm and diameter of 12 μm. The ablation crater depth in such conditions is thus much larger than the deposited films, whatever their thickness. The LIBS signals exhibit linear trends as a function of the film thickness within the 50–700 nm range, itself proportional to the amount of analyte.

This study has successfully demonstrated the ability of LIBS for quantitative analysis of LiPO thin films, as supported by a comparison between LIBS and ICP-OES data. At the same time, we have shown that some Li and P were able to diffuse inside the single crystal substrate, probably only during the early stages of the deposition, this process being at the origin of the non-zero intercept of the LIBS signal as a function of the film thickness.

Outstanding sensitivity of LIBS was evidenced for lithium through the analysis of material amount equivalent to a 4 nm thick LiPO layer, which corresponds to <0.2% of the laser ablation crater volume and to around $0.15 \cdot 10^{-12}$ g of lithium.

These results validate LIBS as a quantitative analysis technique to be implemented in HTE workflows and open the way for the effective exploration of new material systems, such as ion conductive glasses and glass-ceramics with more complex compositions, i.e. based on mixed glass-formers [48,49], or including light elements, such as boron [50]. This study also demonstrates the ability of LIBS to analyse very thin samples, hence its great interest in the study of nanometre-thick films such as those prepared by Atomic Layer Deposition (ALD) [51,52].

CRediT authorship contribution statement

William Berthou: Writing – original draft, Investigation, Data curation. **Maxime Legallais:** Writing – review & editing. **Bruno Bousquet:** Writing – review & editing, Writing – original draft, Investigation. **Vincent Motto-Ros:** Writing – review & editing, Writing – original draft, Investigation, Data curation. **Frédéric Le Cras:** Writing – review & editing, Writing – original draft, Investigation.

Declaration of competing interest

The authors declare that they have no known competing financial interests or personal relationships that could have appeared to influence the work reported in this paper.

Data availability

Data will be made available on request.

Appendix A. Supplementary data

Supplementary data to this article can be found online at https://doi.org/10.1016/j.sab.2024.106906.

References

[1] R. Potyrailo, K. Rajan, K. Stoewe, I. Takeuchi, B. Chisholm, H. Lam, Combinatorial and high-throughput screening of materials libraries: review of state of the art, ACS Comb. Sci. 13 (6) (2011) 579–633, https://doi.org/10.1021/co200007w.

[2] K. McCullough, T. Williams, K. Mingle, P. Jamshidi, J. Lauterbach, High-throughput experimentation meets artificial intelligence: a new pathway to catalyst discovery, Phys. Chem. Chem. Phys. 22 (20) (2020) 11174–11196, https://doi.org/10.1039/D0CP00972E.

[3] A. Benayad, D. Diddens, A. Heuer, A.N. Krishnamoorthy, M. Maiti, F. Le Cras, M. Legallais, F. Rahmanian, Y. Shin, H. Stein, M. Winter, C. Wölke, P. Yan, I. Cekic-Laskovic, High-throughput experimentation and computational freeway lanes for accelerated battery electrolyte and interface development research, Adv. Energy Mater. 12 (17) (2022) 2102678, https://doi.org/10.1002/aenm.202102678.

[4] J.J. Hanak, The "multiple-sample concept" in material research: synthesis, compositional analysis and testing of entire multicomponent systems, J. Mater. Sci. 5 (1970) 964–971.

[5] S.A. Kube, S. Sohn, D. Uhl, A. Datye, A. Mehta, J. Schroers, Phase selection motifs in high entropy alloys revealed through combinatorial methods: large atomic size difference favors BCC over FCC, Acta Mater. 166 (2019) 677–686, https://doi.org/10.1016/j.actamat.2019.01.023.

[6] Y. Liu, J. Padmanabhan, B. Cheung, J. Liu, Z. Chen, B.E. Scanley, D. Wesolowski, M. Pressley, C.C. Broadbridge, S. Altman, U.D. Schwarz, T.R. Kyriakides, J. Schroers, Combinatorial development of antibacterial Zr-Cu-Al-Ag thin film metallic glasses, Sci. Rep. 6 (1) (2016) 26950, https://doi.org/10.1038/srep26950.

[7] P.P. Rajbhandari, A. Bikowski, J.D. Perkins, T.P. Dhakal, A. Zakutayev, Combinatorial sputtering of Ga-doped (Zn,Mg)O for contact applications in solar cells, Sol. Energy Mater. Sol. Cells 159 (2017) 219–226, https://doi.org/10.1016/j.solmat.2016.09.003.

[8] F. Kurokawa, A. Mori, Y. Tsujiura, H. Hida, I. Kanno, Compositional dependence of Ba(Zr0.2Ti0.8)O3–(Ba0.7Ca0.3)TiO3 piezoelectric thin films prepared by combinatorial sputtering, Thin Solid Films 588 (2015) 34–38, https://doi.org/10.1016/j.tsf.2015.04.050.

[9] A.N. Fioretti, A. Zakutayev, H. Moutinho, C. Melamed, J.D. Perkins, A.G. Norman, M. Al-Jassim, E.S. Toberer, A.C. Tamboli, Combinatorial insights into doping control and transport properties of zinc tin nitride, J. Mater. Chem. C 3 (42) (2015) 11017–11028, https://doi.org/10.1039/C5TC02663F.

[10] S.-Y. Hsu, Y.-T. Lai, S.-Y. Chang, S.-Y. Tsai, J.-G. Duh, Combinatorial synthesis of reactively co-sputtered high entropy nitride (HfNbTiVZr)N coatings: microstructure and mechanical properties, Surf. Coat. Technol. 442 (2022) 128564, https://doi.org/10.1016/j.surfcoat.2022.128564.

[11] A. Mockute, J. Palisaitis, N. Nedfors, P. Berastegui, E. Broitman, B. Alling, L.-Å. Näslund, L. Hultman, J. Patscheider, U. Jansson, P.O.Å. Persson, J. Rosen, Synthesis and characterization of (Ti1-XAlx)B2+Δ thin films from combinatorial magnetron sputtering, Thin Solid Films 669 (2019) 181–187, https://doi.org/10.1016/j.tsf.2018.10.042.

[12] R.R. Schnepf, M.B. Tellekamp, T. Saenz, J.S. Mangum, E. Supple, D.M. Roberts, C. L. Perkins, K.N. Heinselman, B.P. Gorman, A.L. Greenaway, E.S. Toberer, A. C. Tamboli, Epitaxial ZnGeP2 thin films on Si and GaP by reactive combinatorial sputtering in phosphine, Cryst. Growth Des. 22 (10) (2022) 6131–6139, https://doi.org/10.1021/acs.cgd.2c00723.

[13] R. Woods-Robinson, Y. Han, J.S. Mangum, C.L. Melamed, B.P. Gorman, A. Mehta, K.A. Persson, A. Zakutayev, Combinatorial tuning of structural and optoelectronic properties in CuxZn1−xS, Matter 1 (4) (2019) 862–880, https://doi.org/10.1016/j.matt.2019.06.019.

[14] T.D. Hatchard, J.M. Topple, M.D. Fleischauer, J.R. Dahn, Electrochemical performance of SiAlSn films prepared by combinatorial sputtering, Electrochem. Solid-State Lett. 6 (7) (2003) A129, https://doi.org/10.1149/1.1574231.

[15] J.R. Dahn, S. Trussler, T.D. Hatchard, A. Bonakdarpour, J.R. Mueller-Neuhaus, K. C. Hewitt, M. Fleischauer, Economical sputtering system to produce large-size composition-spread libraries having linear and orthogonal stoichiometry variations, Chem. Mater. 14 (8) (2002) 3519–3523, https://doi.org/10.1021/cm020236x.

[16] S. Borhani-Haghighi, High-Throughput Compositional and Structural Evaluation of a Lia(NixMnyCoz)Or Thin Film Battery Materials Library, ACS Comb. Sci. 15 (8) (2023) 401, https://doi.org/10.1021/co4000166.

[17] S. Müller, J.A. Meima, Mineral classification of lithium-bearing pegmatites based on laser-induced breakdown spectroscopy: application of semi-supervised learning to detect known minerals and unknown material, Spectrochim. Acta B At. Spectrosc. 189 (2022) 106370, https://doi.org/10.1016/j.sab.2022.106370.

[18] C. Fabre, D. Devismes, S. Moncayo, F. Pelascini, F. Trichard, A. Lecomte, B. Bousquet, J. Cauzid, V. Motto-Ros, Elemental imaging by laser-induced breakdown spectroscopy for the geological characterization of minerals, J. Anal. At. Spectrom. 33 (8) (2018) 1345–1353, https://doi.org/10.1039/C8JA00048D.

[19] C.R. Ytsma, M.D. Dyar, Accuracies of lithium, boron, carbon, and sulfur quantification in geological samples with laser-induced breakdown spectroscopy in Mars, Earth, and vacuum conditions, Spectrochim. Acta B At. Spectrosc. (2019) 162, https://doi.org/10.1016/j.sab.2019.105715.

[20] V. Gardette, V. Motto-Ros, C. Alvarez-Llamas, L. Sancey, L. Duponchel, B. Busser, Laser-induced breakdown spectroscopy imaging for material and biomedical applications: recent advances and future perspectives, Anal. Chem. 95 (1) (2023) 49–69, https://doi.org/10.1021/acs.analchem.2c04910.

[21] S. Richiero, C. Sandoval, C. Oberlin, A. Schmitt, J.-C. Lefevre, A. Bensalah-Ledoux, D. Prigent, C. Coquidé, A. Valois, F. Giletti, F. Pelascini, L. Duponchel, P. Dugourd, C. Comby-Zerbino, V. Motto-Ros, Archaeological mortar characterization using laser-induced breakdown spectroscopy (LIBS) imaging microscopy, Appl. Spectrosc. 76 (8) (2022) 978–987, https://doi.org/10.1177/00037028211071141.

[22] N. Hausmann, A.L. Prendergast, A. Lemonis, J. Zech, P. Roberts, P. Siozos, D. Anglos, Extensive elemental mapping unlocks Mg/Ca ratios as climate proxy in seasonal records of mediterranean limpets, Sci. Rep. 9 (1) (2019) 3698, https://doi.org/10.1038/s41598-019-39959-9.

[23] N. Hausmann, D. Theodoraki, V. Piñon, P. Siozos, A. Lemonis, D. Anglos, Applying laser induced breakdown spectroscopy (LIBS) and elemental imaging on marine shells for archaeological and environmental research, Sci. Rep. 13 (1) (2023) 19812, https://doi.org/10.1038/s41598-023-46453-w.

[24] Y. Murakami, Y. Matsuzaki, T. Kamimura, T. Nishiura, K. Masuda, A. Shibayama, R. Inoue, Erosion mechanism of refractories in a pyro-processing furnace for recycling lithium-ion secondary batteries, Ceram. Int. 46 (7) (2020) 9281–9288, https://doi.org/10.1016/j.ceramint.2019.12.182.

[25] V. Merk, D. Huber, L. Pfeifer, S. Damaske, S. Merk, W. Werncke, M. Schuster, Discrimination of automotive glass by conjoint Raman and laser-induced breakdown spectroscopy and multivariate data analysis, Spectrochim. Acta B At. Spectrosc. 180 (2021) 106198, https://doi.org/10.1016/j.sab.2021.106198.

[26] M.T. Sweetapple, S. Tassios, Laser-induced breakdown spectroscopy (LIBS) as a tool for in situ mapping and textural interpretation of lithium in pegmatite minerals, Am. Mineral. 100 (10) (2015) 2141–2151, https://doi.org/10.2138/am-2015-5165.

[27] M. Kappeler, C. Basler, A. Brandenburg, D. Carl, J. Wöllenstein, Homogeneity measurements of Li-ion battery cathodes using laser-induced breakdown spectroscopy, Sensors 22 (22) (2022) 8816, https://doi.org/10.3390/s22228816.

[28] P. Smyrek, J. Pröll, H.J. Seifert, W. Pfleging, Laser-induced breakdown spectroscopy of laser-structured li(NiMnCo)O$_2$ electrodes for lithium-ion batteries, J. Electrochem. Soc. 163 (2) (2016) A19–A26, https://doi.org/10.1149/2.0981514jes.

[29] H. Hou, L. Cheng, T. Richardson, G. Chen, M. Doeff, R. Zheng, R. Russo, V. Zorba, Three-dimensional elemental imaging of Li-ion solid-state electrolytes using Fs-laser induced breakdown spectroscopy (LIBS), J. Anal. At. Spectrom. 30 (11) (2015) 2295–2302, https://doi.org/10.1039/C5JA00250H.

[30] L. Cheng, E.J. Crumlin, W. Chen, R. Qiao, H. Hou, S. Franz Lux, V. Zorba, R. Russo, R. Kostecki, Z. Liu, K. Persson, W. Yang, J. Cabana, T. Richardson, G. Chen, M. Doeff, The origin of high electrolyte–electrode interfacial resistances in lithium cells containing garnet type solid electrolytes, Phys. Chem. Chem. Phys. 16 (34) (2014) 18294–18300, https://doi.org/10.1039/C4CP02921F.

[31] J.S. Syzdek, V. Zorba, X. Mao, R.E. Russo, R.M. Kostecki, Ultrafast laser spectroscopy of electrode/electrolyte interfaces, ECS Trans. 50 (1) (2013) 39–48, https://doi.org/10.1149/05001.0039ecst.

[32] S. Imashuku, H. Taguchi, T. Kawamata, S. Fujieda, S. Kashiwakura, S. Suzuki, K. Wagatsuma, Quantitative lithium mapping of lithium-ion battery cathode using laser-induced breakdown spectroscopy, J. Power Sources 399 (2018) 186–191, https://doi.org/10.1016/j.jpowsour.2018.07.088.

[33] M.-C. Michaud Paradis, F.R. Doucet, S. Rousselot, A. Hernández-García, K. Rifai, O. Touag, L.Ç. Özcan, N. Azami, M. Dollé, Deep learning classification of Li-ion battery materials targeting accurate composition classification from laser-induced breakdown spectroscopy high-speed analyses, Batteries 8 (11) (2022) 231, https://doi.org/10.3390/batteries8110231.

[34] X. Yu, J.B. Bates, G.E. Jellison, F.X. Hart, A stable thin-film lithium electrolyte: lithium phosphorus oxynitride, J. Electrochem. Soc. 144 (2) (1997) 524, https://doi.org/10.1149/1.1837443.

[35] F. Le Cras, B. Pecquenard, V. Dubois, V.-P. Phan, D. Guy-Bouyssou, All-solid-state lithium-ion microbatteries using silicon nanofilm anodes: high performance and memory effect, Adv. Energy Mater. 5 (19) (2015) 1501061, https://doi.org/10.1002/aenm.201501061.

[36] J. Su, M. Pasta, Z. Ning, X. Gao, P.G. Bruce, C.R.M. Grovenor, Interfacial modification between argyrodite-type solid-state electrolytes and Li metal anodes using LiPON interlayers, Energy Environ. Sci. (2022), https://doi.org/10.1039/d2ee01390h.

[37] S. Shrestha, J. Kim, J. Jeong, H.J. Lee, S.C. Kim, H.J. Hah, K. Oh, S.-H. Lee, Effect of amorphous LiPON coating on electrochemical performance of LiNi0.8Mn0.1Co0.1O2 (NMC811) in all solid-state batteries, J. Electrochem. Soc. 168 (6) (2021) 060537, https://doi.org/10.1149/1945-7111/ac0b28.

[38] V. Lacivita, A. Westover, A. Kercher, N. Phillip, G. Yang, G. Veith, G. Ceder, N. Dudney, Resolving the amorphous structure of lithium phosphorus oxynitride (Lipon), J. Am. Chem. Soc. (2018) 140, https://doi.org/10.1021/jacs.8b05192.

[39] P. Henkel, J. Janek, D. Mollenhauer, Influence of the POuN4−u structural units on the formation energies and transport properties of lithium phosphorus oxynitride: a DFT study, Phys. Chem. Chem. Phys. 23 (39) (2021) 22567–22588, https://doi.org/10.1039/D1CP01294K.

[40] J.O. Cáceres, F. Pelascini, V. Motto-Ros, S. Moncayo, F. Trichard, G. Panczer, A. Marín-Roldán, J.A. Cruz, I. Coronado, J. Martín-Chivelet, Megapixel multi-elemental imaging by laser-induced breakdown spectroscopy, a technology with considerable potential for paleoclimate studies, Sci. Rep. 7 (1) (2017) 5080, https://doi.org/10.1038/s41598-017-05437-3.

[41] I. Jõgi, J. Ristkok, J. Butikova, J. Raud, P. Paris, LIBS plasma in atmospheric pressure argon, nitrogen and helium: spatio-temporal distribution of plume emission and Hα linewidth, Nucl. Mater. Energy 37 (2023) 101543, https://doi.org/10.1016/j.nme.2023.101543.

[42] R. Hai, Z. He, X. Yu, L. Sun, D. Wu, H. Ding, Comparative study on self-absorption of laser-induced tungsten plasma in air and in argon, Opt. Express 27 (3) (2019) 2509, https://doi.org/10.1364/OE.27.002509.

[43] V. Motto-Ros, S. Moncayo, F. Trichard, F. Pelascini, Investigation of signal extraction in the frame of laser induced breakdown spectroscopy imaging, Spectrochim. Acta B At. Spectrosc. 155 (2019) 127–133, https://doi.org/10.1016/j.sab.2019.04.004.

[44] A. Ruzin, N. Abrosimov, P. Litovchenko, Study of lithium diffusion into silicon–germanium crystals, Nucl. Instrum. Methods Phys. Res., Sect. A 617 (1–3) (2010) 588–590, https://doi.org/10.1016/j.nima.2009.10.026.

[45] C.J. Wen, R.A. Huggins, Chemical diffusion in intermediate phases in the lithium-silicon system, J. Solid State Chem. 37 (3) (1981) 271–278, https://doi.org/10.1016/0022-4596(81)90487-4.

[46] Y.M. Haddara, B.T. Folmer, M.E. Law, T. Buyuklimanli, Accurate measurements of the intrinsic diffusivities of boron and phosphorus in silicon, Appl. Phys. Lett. 77 (13) (2000) 1976–1978, https://doi.org/10.1063/1.1313248.

[47] M. Milán, P. Lucena, L.M. Cabalín, J.J. Laserna, Depth profiling of phosphorus in photonic-grade silicon using laser-induced breakdown spectrometry, Appl. Spectrosc. 52 (3) (1998) 444–448, https://doi.org/10.1366/0003702981943662.

[48] T. Famprikis, J. Galipaud, O. Clemens, B. Pecquenard, F. Le Cras, Composition dependence of ionic conductivity in LiSiPO(N) thin-film electrolytes for solid-state batteries, ACS Appl. Energy Mater. 2 (7) (2019) 4782–4791, https://doi.org/10.1021/acsaem.9b00415.

[49] A. Moguš-Milanković, K. Sklepić, P. Mošner, L. Koudelka, P. Kalenda, Lithium-ion mobility in quaternary boro–germano–phosphate glasses, J. Phys. Chem. B 120 (16) (2016) 3978–3987, https://doi.org/10.1021/acs.jpcb.6b01424.

[50] C. Park, S. Lee, S. Choi, D. Shin, Effect of boron/phosphorus ratio in lithium boron phosphorus oxynitride thin film electrolytes for all-solid-state thin film batteries, Thin Solid Films 685 (2019) 434–439, https://doi.org/10.1016/j.tsf.2019.06.055.

[51] A.J. Pearse, T.E. Schmitt, E.J. Fuller, F. El-Gabaly, C.-F. Lin, K. Gerasopoulos, A. C. Kozen, A.A. Talin, G. Rubloff, K.E. Gregorczyk, Nanoscale solid state batteries enabled by thermal atomic layer deposition of a lithium polyphosphazene solid state electrolyte, Chem. Mater. 29 (8) (2017) 3740–3753, https://doi.org/10.1021/acs.chemmater.7b00805.

[52] A.C. Kozen, A.J. Pearse, C.-F. Lin, M. Noked, G.W. Rubloff, Atomic layer deposition of the solid electrolyte LiPON, Chem. Mater. 27 (15) (2015) 5324–5331, https://doi.org/10.1021/acs.chemmater.5b01654.